Depth dependence of vascular fluorescence imaging

Mitchell A. Davis,[1,*] **S. M. Shams Kazmi,**[2] **Adrien Ponticorvo,**[2] **and Andrew K. Dunn**[2]

[1]*Department of Electrical and Computer Engineering, The University of Texas at Austin, Austin, Texas 78712, USA*
[2]*Department of Biomedical Engineering, The University of Texas at Austin, Austin, TX 78712, USA*
*mitch.davis@utexas.edu

Abstract: *In vivo* surface imaging of fluorescently labeled vasculature has become a widely used tool for functional brain imaging studies. Techniques such as phosphorescence quenching for oxygen tension measurements and indocyanine green fluorescence for vessel perfusion monitoring rely on surface measurements of vascular fluorescence. However, the depth dependence of the measured fluorescence signals has not been modeled in great detail. In this paper, we investigate the depth dependence of the measured signals using a three-dimensional Monte Carlo model combined with high resolution vascular anatomy. We found that a bulk-vascularization assumption to modeling the depth dependence of the signal does not provide an accurate picture of penetration depth of the collected fluorescence signal in most cases. Instead the physical distribution of microvasculature, the degree of absorption difference between extravascular and intravascular space, and the overall difference in absorption at the excitation and emission wavelengths must be taken into account to determine the depth penetration of the fluorescence signal. Additionally, we found that using targeted illumination can provide for superior surface vessel sensitivity over wide-field illumination, with small area detection offering an even greater amount of sensitivity to surface vasculature. Depth sensitivity can be enhanced by either increasing the detector area or increasing the illumination area. Finally, we see that excitation wavelength and vessel size can affect intra-vessel sampling distribution, as well as the amount of signal that originates from inside the vessel under targeted illumination conditions.

© 2011 Optical Society of America

References and links

1. J. Rao, A. Dragulescu-Andrasi and H. Yao, "Fluorescence imaging *in vivo*: recent advances," Curr. Opin. Biotech. **18**, 17–25 (2007).
2. L. Cohen and B. Salzberg, "Optical measurement of membrane potential," Rev. Physiol. Biochem. Pharmacol. **83**, 36–77 (1978). .
3. S. Arridge, M. Cope, and D. Delpy, "The theoretical basis for the determination of optical pathlengths in tissue: temporal and frequency analysis," Phys. Med. Biol. **37**, 1531–1560 (1992).
4. D. Hattery, V. Chernomordik, M. Loew, I. Gannot, and A. Gandjbakhche, "Analytical solutions for time-resolved fluorescence lifetime imaging in a turbid medium such as tissue," J. Opt. Soc. Am. A. **18**, 1523–1530 (2001).

5. V. Soloviev, D. Wilson, and S. Vinogradov, "Phosphorescence lifetime imaging in turbid media: the forward problem," Appl. Opt. **42**, 113–123 (2003).
6. I. Dunphy, S. A. Vinogradov, and D. F. Wilson, "Oxyphor R2 and G2: phosphors for measuring oxygen by oxygen-dependent quenching of phosphorescence," Anal. Biochem. **310**, 191-198 (2002).
7. M. L. Landsman, G. Kwant, G. A. Mook, and W. G. Zijlstra, "Light-absorbing properties, stability, and spectral stabilization of indocyanine green." J. Appl. Physiol. **40**, 575-583 (1976).
8. D. F. Wilson, S. A. Vinogradov, P. Grosul, M. N. Vaccarezza, A. Kuroki, and J. Bennett, "Oxygen distribution and vascular injury in the mouse eye measured by phosphorescence-lifetime imaging," Appl. Opt. **44**, 5239–5248 (2005).
9. S. A. Vinogradov, M. A. Fernandez-searra, B. W. Dugan, and D. A. Wilson, "Frequency domain instrument for measuring phosphorescence lifetime distributions in heterogeneous samples," Rev. Sci. Instrum. **72**, 3396–3406 (2001).
10. R. D. Shonat and P. C. Johnson, "Oxygen tension gradients and heterogeneity in venous microcirculation: a phosphorescence quenching study," Am. J. Physiol. Heart. Ciculatory Physiol. **272**(5), H2233–H2240 (1997).
11. M. A. Yaseen, V. J. Srinivasan, S. Sakadžić, W. Wu, S. Ruvinskaya, S. A. Vinogradov, and D. A. Boas, "Optical monitoring of oxygen tension in cortical microvessels with confocal microscopy," Opt. Express **17**, 22341–22350 (2009).
12. A. Raabe, J. Beck, R. Gerlach, M. Zimmerman, and V. Seirfert, "Near-infrared indocyanine green video angiography: a new method for intraoperative assessment of vascular flow," Neurosurgery **52**, 132-139 (2003).
13. A. Ponticorvo and A. K. Dunn, "Simultaneous imaging of oxygen tension and blood flow in animals using a digital micromirror device," Opt. Express **18**, 8160–8170 (2010).
14. M. A. Yaseen, V. J. Srinivasan, S. Sakadžić, H. Radhakrishnan, I. Gorczynska, W. Wu, J. G. Fujimoto, and D. A. Boas, "Microvascular oxygen tension and flow measurements in rodent cerebral cortex during baseline conditions and functional activation," J. Cerebr. Blood Flow Metabol. **31**, 1051-1063 (2010).
15. V. Y. Soloviev, D. F. Wilson, and S. A. Vinogradov, "Phosphorescence lifetime imaging in turbid media: the inverse problem and experimental image reconstruction," Appl. Opt. **43**, 564–574 (2004).
16. P. Tian, A. Devor, S. Sakadžić, A.M. Dale, and D.A. Boas, "Monte Carlo simulation of the spatial resolution and depth sensitivity of two-dimensional optical imaging of the brain," J. Biomed. Opt. **16**, 016006 (2011).
17. C. K. Hayakawa, J. Spanier, F. Bevilacqua, A. K. Dunn, J. S. You, B. J. Tromberg, and V. Venugopalan, "Perturbation Monte Carlo methods to solve inverse photon migration problems in heterogeneous tissues," Opt. Lett. **26**, 1335–1337 (2001).
18. A. Kumar, J. Skoch, B. Bacskai, D. Boas, and A. Dunn, "Fluorescence-lifetime-based tomography for turbid media," Opt. Lett. **30**, 3347–3349 (2005).
19. T. Pfefer, J. Kehlet Barton, E. Chan, M. Ducros, B. Sorg, T. Milner, J. Nelson, and A.J. Welch, "A three-dimensional modular adaptable grid numerical model for light propagation during laser irradiation of skin tissue," IEEE J. Sel. Top. Quantum Electron. **2**, 934–942 (1996).
20. J. Barton, T. Pfefer, A. Welch, D. Smithies, J. Nelson, and M. Van Gemert, "Optical Monte Carlo modeling of a true portwine stain anatomy," Opt. Express **2**, 391–396 (1998).
21. F. E. Robles, S. Chowdhury, and A. Wax, "Assessing hemoglobin concentration using spectroscopic optical coherence tomography for feasibility of tissue diagnostics," Opt. Express **1**, 310–317 (2010).
22. F. Bevilacqua, D. Piguet, P. Marquet, J. D. Gross, B. J. Tromberg, and C. Depeursinge, "*In vivo* local determination of tissue optical properties: applications to human brain," Appl. Opt. **38**, 4939–4950 (1999).
23. M. Friebel, K. Do, A. Hahn, G. Mu, D. Berlin, L. Medizin, and F. Universita, "Optical properties of circulating human blood in the wavelength range 400–2500 nm," J. Biomed. Opt. **4**, 36–46 (1999).
24. A. N. Yaroslavsky, P. C. Schulze, I. V. Yaroslavsky, R. Schober, F. Ulrich, and H. J. Schwarzmaier, "Optical properties of selected native and coagulated human brain tissues in vitro in the visible and near infrared spectral range," Phys. Med. Biol. **47**, 2059–2073 (2002).
25. A. Sassaroli, C. Blumetti, F. Martelli, L. Alianelli, D. Contini, A. Ismaelli, and G. Zaccanti, "Monte Carlo procedure for investigating light propagation and imaging of highly scattering media." Appl. Opt. **37**, 7392–7400 (1998).

---

1. Introduction

Fluorescence imaging is widely used for measuring functional and structural parameters which cannot be easily imaged using endogenous sources of contrast. The specific uses of fluorophores and phosphors *in vivo* vary widely; a few examples include applications such as molecular imaging, cancer imaging, and functional imaging of hemodynamic properties [1]. Correspondingly, there are a number of delivery methods for fluorophores depending on the application in question.

Several imaging methods require the topical application of fluorophores, and subsequent

diffusion through the tissue prior to imaging. An example of this method is voltage sensitive dye (VSD) imaging, which is often used to image changes in membrane potential [2]. When not considering the genetically expressed protein variants, these methods are inherently limited by both the capability of the fluorophore to diffuse through the tissue, and the need to excite the fluorophore and measure the emission through the highly turbid tissue media. However, as these agents distribute themselves in the tissue via diffusion, predicting the distribution of the agent in the tissue can typically be done through the diffusion equation [3].

Intravascular contrast agents do not suffer from the need to diffuse through tissue, as they can be administered intravenously. However, imaging is more difficult to model mathematically as the fluorophore is no longer distributed in a smooth gradient, as is generally the assumption with topically applied contrast agents. Several analytical methods have been used to model photon migration in an *in vivo* fluorescence imaging context. All of these methods treat the tissue as a homogeneous medium, or a series of homogeneous layers, where transport theory determines the depth and resolution of imaging [3–5]. These methods are not intended to predict fluorescence emission when the fluorophore distribution is determined by the vasculature.

As such, the purpose of our paper is to analyze the depth dependence of the measured signal in intravascular fluorescence imaging using two common dyes: Pd-porphyrin based phosphorescence [6] and indocyanine green (ICG) [7]. The Pd-porphyrin considered here is an oxygen sensitive phosphorescent probe which has excitation maximas at 415 and 524 nm, and an emission maximum at 690 nm [6]. This probe is widely used for measuring intravascular oxygen tension *in vivo* [8–10]. ICG is a fluorescent probe used to image blood vessel perfusion in a number of surgical applications [12], and has an absorption maximum in plasma at approximately 800 nm, and an emission maximum at 880 nm. While these dyes are specific, their excitation and emission wavelength optical properties are comparable to many other intravascular contrast agents.

We have developed a Monte Carlo model whereby fluorescence emission can be modeled in a realistic *in vivo* geometry using excitation and detection schemes currently being used [13–15]. The model is used to determine the differences in fluorescence emission distribution between a realistic microvasculature geometry and a homogeneous tissue geometry. The model is further used to demonstrate the origin of fluorescence emission under several different illumination and detection schemes, and then to study intra-vessel distribution of fluorescence emission based on the excitation wavelength.

Recent work by Tian et. al. [16] used Monte Carlo simulations to study spatial resolution and depth dependent sensitivity to perturbations in both fluorescent and non-fluorescent two dimensional imaging using a homogeneous tissue geometry. Our work, however, focuses on the *origin* and spatial distribution of detected fluorescence which originates specifically in the vasculature.

2. 3D fluorescence Monte Carlo model

The model uses a 3D fluorescence Monte Carlo method to evaluate an illumination and detection scheme in an arbitrary geometry [17, 18]. Similar non-fluorescence based modeling techniques [19] have been used to study port-wine stain in an epidermal geometry obtained via optical coherence tomography [20]. Geometries are specified by setting tissue optical properties in a 3D voxelized grid. Optical properties for each voxel can be specified for both the excitation light and the emitted light. The modeled excitation photons scatters through the tissue and can either be absorbed in a voxel, whereby an emission event may occur, or terminated if it reaches the boundary of the geometry. Emission photons originate from the location of absorption and are emitted isotropically. The emitted photons can then either scatter or be absorbed based on an independent set of emission optical properties.

2.1. Geometry and optical properties

The optical properties of Pd-porphyrin, ICG, blood and gray matter were used in this model. The Monte Carlo model allowed for an arbitrary 3D voxelized geometry, where each voxel could represent one of up to 255 different sets of optical properties (μ_a, μ_s, g). Quantum efficiency can be set for the emission optical properties, which determines the likelihood of fluorescence or phosphorescence emission upon absorption of an incident excitation photon.

The model geometry was derived from *in vivo* images of mouse cortical vasculature. Scanning two-photon fluorescence microscopy was used to generate depth-resolved stacks of microvasculature in a mouse (CD-1; male, 25 - 30 g). All experimental procedures were approved by the Institutional Animal Care and Use Committee (IACUC) at the University of Texas at Austin. The animals were anesthetized by inhalation of 2.3% isoflurane in oxygen through a nose cone. Body temperature was maintained at 37° C using a feedback controlled heating plate (ATC100, World Percision Instruments, Sarasota, FL, USA) during the experiment. The animals were fixed in a stereotaxic frame (Kopf Instruments, Tujunga, CA, USA) and an 3mm x 3mm portion of the skull was removed using a dental burr (IdealTM Micro-Drill, Fine Science tools, Foster City, CA, USA). 50μL of 5% weight/volume Texas Red (Invitrogen, Eugene, OR, USA) was administered through a retro-orbital injection to label the vasculature. A $500\,\mu$m $\times 500\,\mu$m image was taken in $2\,\mu$m z-steps down to $400\,\mu$m. The geometry for the Monte Carlo model was then created by filtering the images to smooth out heterogeneities in the vasculature, interpolating to attain images at every $1\,\mu$m and thresholding the images to generate a 500x500x400 voxel binary geometry. Each voxel was assigned a set of excitation and emission optical properties based on whether it represented extravascular or intravascular space. Fig. 1(a) shows the two-photon stack used to generate the geometry.

The intravascular absorption coefficients were generated based on the extinction coefficients of hemoglobin and Pd-porphyrin/ICG. Concentrations of hemoglobin and Pd-porphyrin in the vasculature were assumed to be 2.3 mM [21] and 0.1 mM [13] respectively. The concentration of ICG was 0.13 mM. Scattering coefficients were interpolated from measurements done by Bevilacqua et al. [22] and Friebel et al. [23]. Extravascular absorption and scattering coefficients were based on the *in vitro* measurements by Yaroslavsky et al. [24]. It was necessary to use *in vitro* measurements of the extravascular tissue because blood was assumed to only be present in intravascular space. The *in vitro* measurements were taken in the absence of blood. The
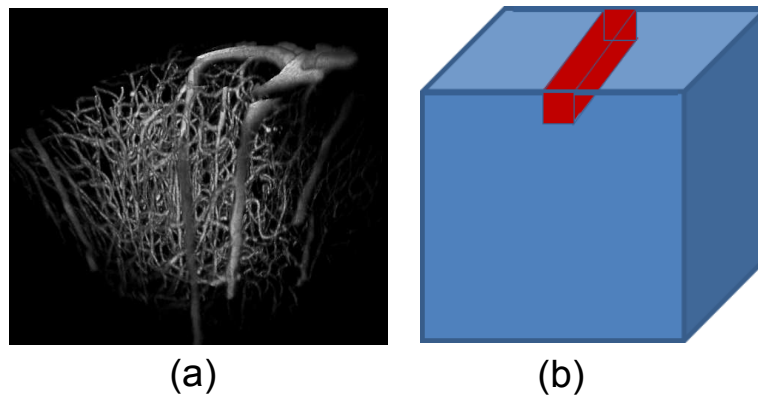

(a)   (b)

Fig. 1. (a) $500\,\mu$m by $500\,\mu$m by $400\,\mu$m microvasculature image stack acquired in a CD-1 mouse brain by two-photon scanning microscopy. (b) Single vessel geometry. Red area represents vessel, blue area represents bulk-vascularized space.

scattering coefficients were found to be slightly higher at 800 nm and 880 nm, which is likely an artifact of ex vivo measurements. The quantum efficiency was set to 1 for the intravascular space and 0 for the extravascular space. Though realistically the quantum efficiency would be 5-10%, the model allowed for 100% conversion of absorbed excitation photons to emission photons in the fluorescing region to increase computational efficiency. Using this model for quantum efficiency is accurate when a single fluorophore is present in the model, and the concentration of fluorophore is the same in all regions containing the fluorophore. Table 1 lists the optical properties used for the microvasculature geometry.

Homogeneous tissue geometries were also created to compare against the realistic geometry. These geometries were created by using a $500 \times 500 \times 400$ voxel geometry where all voxels were assigned the same properties. Optical properties were assigned by assuming that the only absorber was blood mixed with fluorescent dye, the same assumption made for the intravascular properties in the microvasculature geometry. The properties were then scaled by 0.01, 0.05 and 0.10 to represent a bulk-vascularization assumption of 1%, 5% and 10% respectively. The microvasculature geometry used contained approximately 3.5% vascularization, so the chosen bulk-vasculature amounts of 1%, 5% and 10% provide a range of approximattions that can be used for comparison.

Additional geometries were created to determine the effect of targeting a single vessel. A $3mm \times 3mm \times 3mm$ cubic geometry with a single vessel running down the top center was created, as shown in Fig. 1(b). The size of the vessel was varied from $25\,\mu$m to $200\,\mu$m in $25\,\mu$m increments. The intra-vessel optical properties were set according to the values listed in Table 1. Outside the vessel, the tissue was assumed to be homogeneous with a bulk volume fraction of approximately 5%.

2.2. Fluorescence Monte Carlo

A 3D fluorescence Monte Carlo model was used where photons enter the 3D voxelized geometry in a user specified location, beam radius and numerical aperture. Each voxel is assigned

Table 1. Optical properties for microvasculature geometry

	μ_a (mm^{-1})	μ_s (mm^{-1})	g
Pd − porphyrin			
415 nm			
Intravascular	280	180	0.98
Extravascular	0.5	14	0.9
524 nm			
Intravascular	16.3	120	0.98
Extravascular	0.1	11.3	0.9
690 nm			
Intravascular	0.2	100	0.98
Extravascular	0.1	10	0.9
ICG			
800 nm			
Intravascular	3.75	124	0.98
Extravascular	0.1	12.4	0.9
880 nm			
Intravascular	0.7	130	0.98
Extravascular	0.1	13	0.9

optical properties at both the excitation and emission wavelengths. Absorption of excitation photons is handled as an all-or-nothing event to provide a specific location for emission photon generation. If an excitation photon is absorbed, then a fluorescence photon may be generated depending on the quantum efficiency of the tissue type, or voxel, where the photon was absorbed.

Upon creation, the fluorescence photon is emitted isotropically from the point where the excitation photon was absorbed. The model then uses emission optical properties to specify the scattering and step sizes of the fluorescent photons. Absorption is not calculated at each emission photon move location, but is instead applied during post-processing [17, 25]. For each fluorescence photon that exits the tissue within the specified detector area and NA, the total path length traveled in each tissue type is recorded. In post processing, the contribution to the detected signal from photons originating at a point inside the tissue (x, y, z) is calculated as:

$$I_d(x, y, z) = \sum_j e^{-\sum_i \mu_a^i l_{ij}} \tag{1}$$

where j represents the photons originating at point (x, y, z) in the tissue, and i represents the tissue type inside the geometry. The distance each photon travels within each tissue type, l_{ij}, and the absorption coefficient, μ_a^i, in each tissue type is used to generate the weight of each photon using Beer's law. In our simulations, two tissue types were used: vasculature and non-vasculature. Therefore, the total travel lengths in vascular (l_1), and non-vascular (l_2) were saved for each detected fluorescent photon. This process is repeated for every point inside the geometry to build up a three dimensional distribution of signal using photons which arrive at a user specified detector location.

The depth-dependent signal distribution, $f(z)$, which is the probability of the collected signal originating from a depth z in the geometry, was calculated from the signal intensity distribution $I_d(x, y, z)$ using the following relation:

$$f(z) = \frac{\iint I_d(x, y, z) dx dy}{\iiint I_d(x, y, z) dx dy dz} \tag{2}$$

The depth-integrated signal distribution, $F(z)$ can then be calculated by integrating $f(z)$ from 0 to z, and represents the amount of signal originating from the first z in the geometry. The expression for $F(z)$ is as follows:

$$F(z) = \int_0^z f(z) dz \tag{3}$$

2.3. Simulations

2.3.1. Comparison of microvasculature and homogeneous geometry

Our first consideration was to analyze the difference in the spatial distribution of the origin of emission between an *in vivo* microvasculature geometry, and the more typically used assumption of homogeneous tissue with a volume fraction of absorbers. In the microvasculature geometry, a wide field illumination and small detection area method was simulated to mimic a single pixel in a typical camera geometry. A $400\,\mu$m diameter, slightly diverging (NA = 0.01) cone of light on the surface of the tissue geometry was used as the illumination. The detector was a $50\,\mu$m $\times$ $50\,\mu$m square at the top-center of the geometry, which is intended to act similarly to a pixel in a camera. Imaging techniques which rely on a full surface illumination and a camera for detection operate on a similar principle. The small detection volume can be thought

of as a single pixel in a camera. This illumination and detection scheme will henceforth be referred to as the "camera" scheme.

For each of the three homogeneous tissue geometries, 1%, 5%, and 10% blood volume fraction, simulations were performed using 415 nm, 524 nm, and 800 nm excitation. Absorption coefficients in homogeneous areas were set to the intravascular absorption coefficient scaled by the volume fraction. Quantum efficiency was set to 1, as blood was assumed to be the only absorber. The signal intensity as a function of depth was calculated from the results of the simulation, in addition to the cumulative distribution function. As with the microvasculature geometries, the camera scheme was used for illumination and detection. $f(z)$ and $F(z)$ were calculated from the signal distribution, $I_d(x,y,z)$ using Eqns. (2) and (3), and used to compare the homogeneous and microvascular geometries. The effect of detector position on $f(z)$ and $F(z)$ was also investigated at each excitation wavelength by comparing two areas with small pial vessel clusters and one area containing a larger $25\,\mu$m diameter vessel directly on the surface of the microvasculature geometry.

2.3.2. Evaluation of different illumination and detection schemes

For each excitation wavelength (415 nm, 524 nm and 800 nm), the microvascular geometry was used for three illumination and detection schemes. The camera illumination and detection scheme described previously was used for the comparison, in addition to two other methods: the "targeted" scheme, and the "confocal" scheme.

The "targeted" method consisted of a $20\,\mu$m diameter illumination area and a detector that captured all emission photons exiting the surface of the tissue. This scheme mimics selective illumination of a small area of the tissue and integration of all fluorescent photons exiting the tissue, similar to approaches that utilize structured excitation with single point detectors [13].

The third method was a hybrid of the previous two, which is similar to the scanning confocal method. The illumination source was a $20\,\mu$m diameter beam with an NA of 0.01, while the detector was a $50\,\mu$m $\times$ $50\,\mu$m square at the top-center of the geometry. While this method does not mimic true confocal imaging, it does combine small-area illumination with a detector intended to reject light from areas away from the focal volume. As such, we will refer to this method as the "confocal" illumination and detection scheme.

The results of the three illumination schemes were then compared to determine the effect of choosing a targeted illumination scheme over a wide-field illumination scheme, as well as a wide area detector (i.e., PMT or APD) over a small area detector (i.e., camera pixel) based on the desired signal distribution.

To provide a comparison between the schemes, both the depth-dependent and depth-integrated signal distributions for each excitation and emission wavelength pair were calculated according to Eqns. (2) and (3). Additionally, the 3D rendering of the signal distribution for the camera scheme, $I_d(x,y,z)$, was generated and overlaid on the maximum intensity projection of the microvasculature geometry to demonstrate the effects of using a wide field illumination method.

2.3.3. Evaluation of fluorescence sampling in single vessels

The objective of the single vessel geometry was to determine the penetration of excitation light into underlying tissue when fluorescence is measured from surface vessels, and thus to determine how much of the captured signal can be attributed to the targeted vessel. As such, the illumination area was a circle with a diameter that matched the diameter of the vessel in each geometry. Vessel diameters of 25, 50, 75, 100, 150, and $200\,\mu$m were used, which represents approximately the range of vessel diameters in the rat cortex, excluding capillaries, precapillary arterioles, and postcapillary venules. Simulations were performed using 415 nm, 524 nm and

800 nm illumination and a wide area detector. Outside of the vessel, a 5% volume fraction of vascularization was used so that a measure of the amount of excitation light penetrating through the vessel could be easily measured. The portion of the signal $I_d(x,y,z)$ inside the vessel was divided by the total integrated signal to obtain a value representing the percentage of signal originating from inside the single targeted vessel.

3. Results

3.1. Comparison of microvasculature and homogeneous geometry

The comparison between the microvasculature geometry and the homogeneous tissue geometry can be seen in Fig. 2. The top row of Fig. 2 shows the depth-dependent signal distribution, $f(z)$, of the collected signal, calculated using Eq. (2). The bottom row of Fig. 2 shows the depth-integrated signal distribution, $F(z)$, of the collected signal as a function of depth–a value of 0.3 at $100\,\mu$m, therefore, would mean that 30% of the fluorescence signal originated from the top $100\,\mu$m of the geometry.

For reference, measurements of the volume of the microvasculature geometry showed that the approximate volume fraction of blood vessels was 3.5%. Homogenous geometries of 1%, 5%, and 10% for 415 nm and 524 nm excitation and 5% and 10% for 800 nm excitation are shown to demonstrate that the results do not match a realistic geometry in most cases. The results suggest that the accuracy of a bulk-vascularized tissue assumption is strongly dependent on the excitation wavelength of the fluorophore.

The 415 nm excitation case shown in Fig. 2(a-b) shows that the microvasculature geometry model falls between the 1% and 5% homogeneous geometry. The $50\,\mu$m $\times$ $50\,\mu$m detector location is positioned in the center of the illumination ring. The area contains a pial vessel at approximately $40\,\mu$m inside the tissue, which explains the peak at $40\,\mu$m in the plot of $f(z)$.

524 nm and 800 nm excitation produced different results. Fig. 2(c-d) shows that with 524 nm excitation the microvasculature geometry simulation gives a depth-dependent signal distribution less than that of even a 10% vacularized homogeneous tissue geometry. While the 524 nm excitation still shows shallower penetration than would be expected given the 3.5% vascularized geometry used, the error is less dramatic than the 800 nm case. 800 nm excitation with 880nm emission, shown in Fig. 2(e-f) again produced the opposite result from the 415 nm excitation, where the depth penetration is significantly less than what would be expected.

Fig. 3 shows the depth-dependent and depth-integrated signal distributions corresponding to detector locations marked in the maximum intensity projection of the microvasculature stack at (a-b) 415 nm, (c-d) 524 nm and (e-f) 800 nm excitation wavelengths. The two regions chosen which contained small pial vessels, marked in blue and green, had similar depth-integrated distributions. When the detector was positioned over the larger $25\,\mu$m diameter surface vessel, the depth-dependent and depth-integrated distributions were strongly weighted towards the first $25\,\mu$m in the geometry. Approximately 65% of the collected signal originated from the first $25\,\mu$m using 415 nm and 524 nm excitation, and 53% of the signal originated from the same region at 800 nm. From the depth-dependent distribution at 415 nm excitation shown in fig. 3(a), the first 60% of the signal originates from the top $5\,\mu$m of the surface vessel, while the remaining $20\,\mu$m of vessel contributes the other 5% of the signal. At both 524 nm and 800 nm, however, the signal is distributed evenly throughout the surface vessel.

3.2. Evaluation of different illumination and detection schemes

Figure 4 shows the depth dependence of the detected signals for the three imaging geometries. Fig. 4(a-b) shows the depth-dependent and depth-integrated signal distributions in the microvasculature geometry using the camera illumination and detection scheme at 415 nm, 524
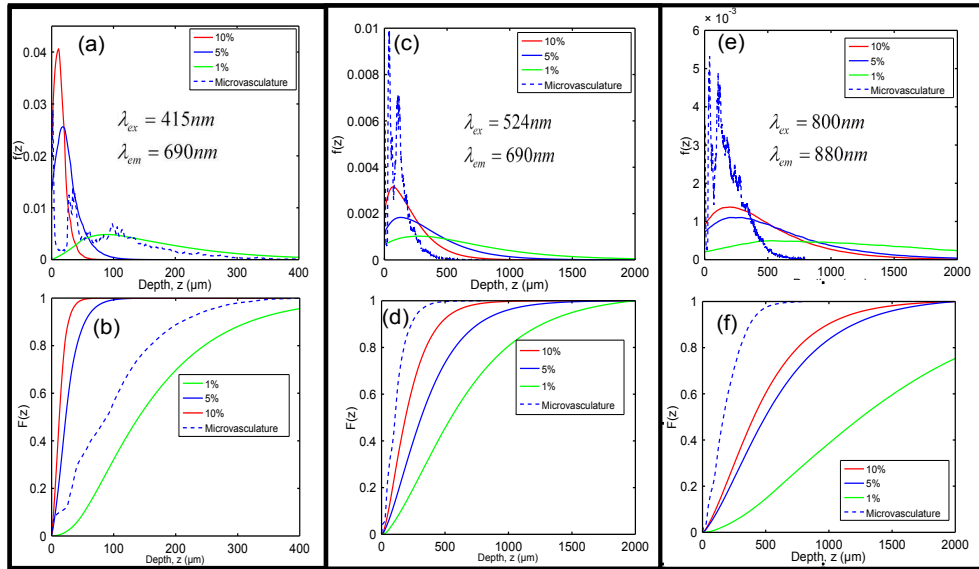
Fig. 2. $f(z)$ and $F(z)$ of collected signal using homogeneous, bulk-vascularized tissue assumption and comparison to the camera illumination and detection scheme using (a-b) 415 nm, (c-d) 524 nm and (e-f) 800 nm excitation. Note that the x-axis in (a-b) is different from (c-f).
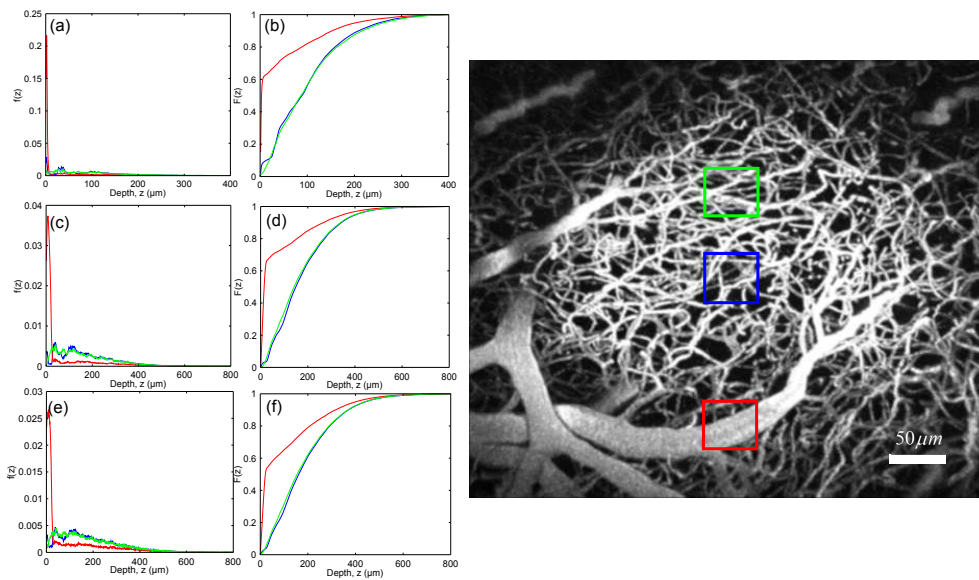

Fig. 3. $f(z)$ and $F(z)$ of collected signal using the camera illumination and detection scheme at different detector positions using (a-b) 415 nm, (c-d) 524 nm and (e-f) 800 nm excitation. Note that the x-axis in (a-b) is different from (c-f).
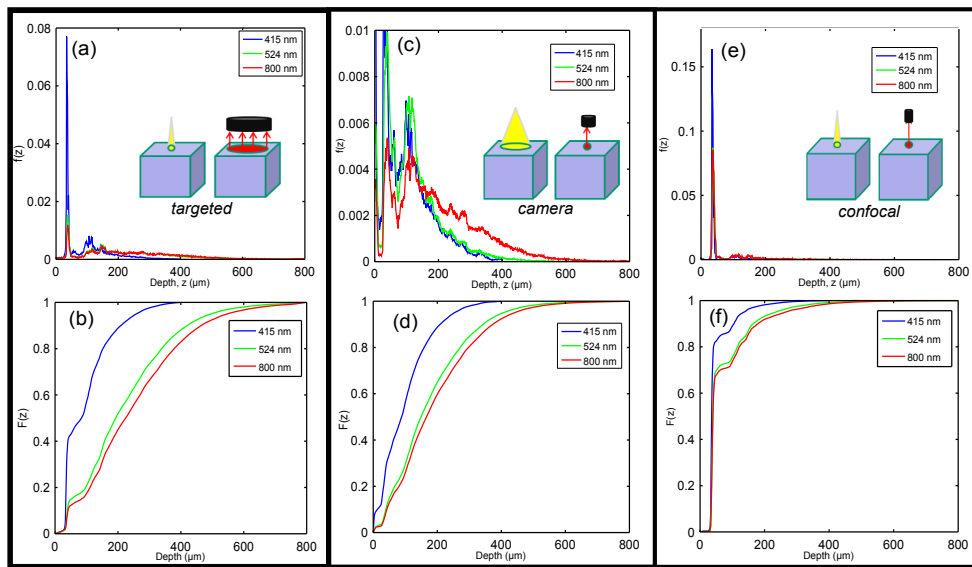
Fig. 4. (a) Depth-dependent, $f(z)$, and (b) depth-integrated, $F(z)$, signal distribution for the targeted illumination and detection scheme; (c) and (d) are $f(z)$ and $F(z)$ using the camera scheme, and (e) and (f) are $f(z)$ and $F(z)$ using the confocal scheme.

nm and 800 nm excitation. Fig. 4(c-d) shows $f(z)$ and $F(z)$ when using a wide-field illumination method with a small detection area on the surface of the tissue, and Fig. 4(e-f) shows $f(z)$ and $F(z)$ in the case of the confocal illumination and detection scheme.

From Fig. 4(e-f), the best spatial localization is obtained when using the confocal illumination and detection scheme. The strong peak at approximately $40\,\mu$m in the plots on the bottom row represents an approximately $20\,\mu$m wide vessel directly below the surface position of the illumination beam and the center of the detector.

Using the targeted scheme, shown in Figs. 4(a-b), generates a strongly wavelength-dependent signal distribution. When using 415 nm excitation, the signal distribution is similar to the distribution obtained when using the confocal illumination and detection scheme. However, when 524 nm or 800 nm excitation light was used, the first vessel encountered did not represent a significant fraction of the total measured signal.

Lastly, the camera scheme shown in Fig. 4(c-d), is the least sensitive method of the three to surface vasculature, with only a small fraction of the total collected signal originating from directly under the detector area.

As a visual aide, Fig. 5 shows the origin of fluorescence detected in a small area on the surface when using the camera illumination and detection scheme, overlaid on top of the maximum intensity projection of the microvasculature stack. The simulation demonstrates that when a large area on the surface is illuminated, the fluorescence signal collected at the surface can originate not only from deeper in the tissue under the detector area, but also from areas near the surface that are not under the detector: similar to what is seen with source-detector separations.

A $50\,\mu$m $\times\,50\,\mu$m $\times\,100\,\mu$m section of the tissue below the detector was evaluated to determine how much of the signal originated from fluorescent photons emitted from $100\,\mu$m below the $50\,\mu$m $\times\,50\,\mu$m detector. At 415 nm, 33.2% of the fluorescence originated from $100\,\mu$m below the detector surface. At 524 nm, 15.6% originated in that area, and at 800 nm, 13.2% of the fluorescence originated within the region. When comparing these results to the total amount of
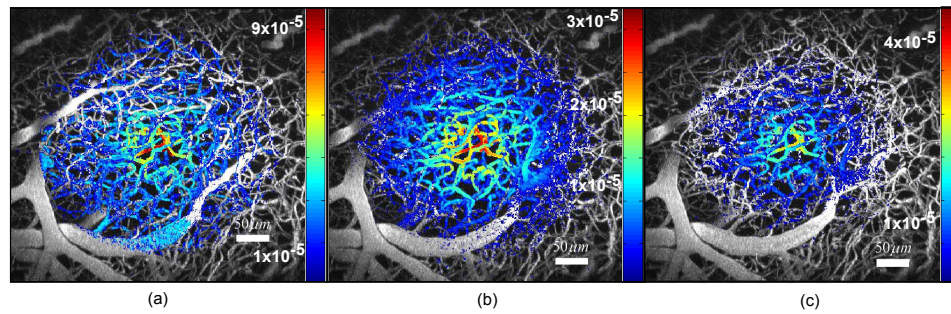
Fig. 5. 3D rendering of fluorescence signal distribution using the camera illumination and detection scheme for (a) 415 nm, (b) 524 nm and (c) 800 nm excitation. Note that the scale bar in (c) is different from (a) and (b).

fluorescence originating from the first $100\,\mu$m of tissue, the fraction of fluorescence originating from below the detector is approximately 50% in all three cases.

3.3. Intra-vessel distribution of fluorescence emission

Fig. 6 shows the results of single vessel geometry simulations at 524 nm and 415 nm illumination. Figs. 6(a) and 6(b) show a simulation result when the vessel size was set to $100\,\mu$m. The 3D distribution of the signal, $I_d(x,y,z)$ was integrated along the length of the vessel to generate the images in Figs. 6(a) and 6(b). A figure demonstrating single vessel penetration of 800 nm excitation light is not shown, as it visually appears similar to the 524 nm excitation case. Fig. 6(c) shows the fraction of the total collected signal which originated inside the $100\,\mu$m vessel at each of the three excitation wavelengths. A targeted surface vessel with a diameter of $100\,\mu$m, for example, will produce a signal that is 100% representative of the vessel fluorescence at 415 nm, 80% representative of vessel fluorescence at 524 nm, and 50% representative of vessel fluorescence at 800 nm.

4. Discussion

4.1. Comparison of microvasculature and homogeneous geometry

From Fig. 2, we found that the microvasculature geometry simulations produce significantly different results than the homogeneous tissue geometry except when considering the camera scheme. Additionally, the excitation wavelength is important when considering *how* the microvasculature geometry is different from the homogeneous geometry. Using 415 nm excitation, as in Fig. 2(a-b), the homogeneous geometry appears to reasonably predict the depth-integrated distribution of the fluorescence signal. However, when upon changing the detector location, as in 3(a-b), it is shown that this is only the case when the detector is positioned over clusters of small pial vessels. When a the detector is positioned over a larger surface vessel, the signal is strongly weighted toward the surface. When 524 nm and 800 nm excitation were used, as in Fig. 2(c-f), the homogeneous geometry over predicted the depth distribution of the emitted fluorescence. Positioning the detector over surface vessels, shown in 3(c-f) only increased the amount of signal originating from the surface of the geometry.

The strongest contributor to $f(z)$ and $F(z)$ appears to be the actual physical distribution of vessels at the detector location. When the detector is positioned over an area containing several small pial vessels, the collected signal does not appear to be significantly weighted towards any particular depth in the tissue. When the detector is positioned over a larger surface vessel, however, the depth-dependent distribution is strongly weighted towards the location
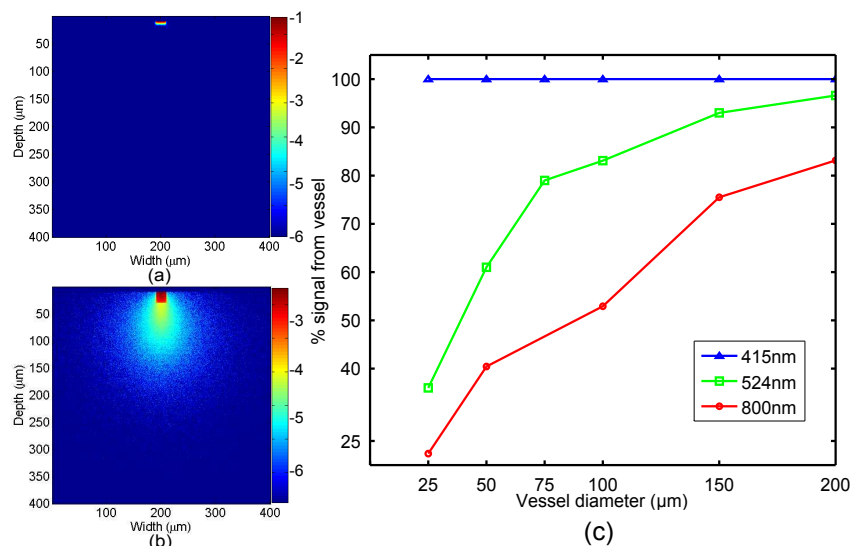
Fig. 6. 100 μm single vessel geometry with (a) 415 nm targeted illumination and (b) 524 nm targeted illumination. Color represents the log of the signal distribution in each 1 μm $\times$ 1 μm pixel. (c) Amount of detected signal originating from inside the vessel as a function of vessel diameter.

of the surface vessel. This difference significantly shifts the depth-integrated distribution of the collected signal towards the surface, and causes the homogeneous geometry assumption to predict the depth penetration even worse than it does when the detector is over smaller pial vessels.

Differences in signal distribution between the microvasculature geometry and the homogeneous tissue geometry can be partially attributed to the large difference between the intra and extra vascular absorption coefficients. Excitation photons experience a small amount of absorption outside of the blood vessels, which allows them to scatter around blood vessels and penetrate deeper into the tissue. The emission photons, being stokes-shifted into the near infrared region for the fluorophores considered here, are not strongly absorbed in any tissue and can return to the surface without much attenuation from absorption.

Additionally, it appears that when positioning the detector over areas containing clusters of small pial vessels, the depth of penetration in a realistic geometry relative to the homogeneous geometry assumption correlates with the amount of difference between the absorption of blood and contrast agent at the excitation wavelength and the emission wavelength. A large excitation-emission absorption difference, such as the 415 nm to 690 nm in Pd-porphyrin, causes the depth penetration to be reasonably predicted by the homogeneous geometry assumption. When there was a smaller difference, as in the 524 nm and 800 nm excitation cases, the homogeneous tissue assumption significantly over predicts the depth of the collected signal distribution. These results are likely unique to the case of intravascular fluorophore distributions and have little bearing on previous numerical studies, where the fluorophore is distributed via diffusion into the tissue [16].

4.2. Evaluation of different illumination and detection schemes

Given the results seen confocal type illumination and detection scheme in 4(e-f), it appears that given a low numerical aperture (NA) beam, surface vasculature can be strongly emphasized by

localizing both the illumination and the detection positions, as in the confocal scheme.

In the targeted illumination scheme, shown in 4(a-b), the fraction of signal originating from the first vessel encountered was highly dependent on the excitation wavelength. This observation could be useful if stronger sensitivity to surface vasculature is desired, as this can be controlled somewhat with selection of excitation wavelength. With Pd-porphyrin, either the surface vasculature can be emphasized by using 415 nm excitation light, or higher depth sensitivity can be obtained by using 524 nm excitation light. Unlike with the camera scheme shown in 3, both the confocal and targeted schemes are able to emphasize the surface-most vessels even when they are small and not directly on the surface.

Regardless of the excitation wavelength used, the light entering the detector in the camera scheme is not representative of the surface-most vessels below the detector area. This is an important observation, as often the surface vasculature will be visible on the camera which is detecting the fluorescence, and it is easy to mistake the signal received as coming from the surface vessels. Fig. 5 provides a good visual aid to explain the peaks in Fig. 2(c). The peaks at the surface correspond to the signal detected from the surface vasculature under the entire illumination area, while the peaks at $40\,\mu$m correspond to the first vessel directly beneath the detector surface. From the results found by analyzing the $50 \times 50 \times 100\,\mu$m box below the detector, the fluorescence originating from below the detector accounts for approximately half of the total fluorescence detected from the first $100\,\mu$m, regardless of the wavelength used. The remainder of the signal originates from areas deeper than $100\,\mu$m, as well as in the first $100\,\mu$m of tissue but outside the $50\,\mu$m $\times 50\,\mu$m detector area.

From Fig. 4, the results suggest that techniques which prioritize accurate imaging of microvasculature should aim to focus the excitation light on the tissue of interest. If the excitation light has a small NA (nearly collimated), then the emitted light will represent vasculature at a number of different depths, dependent on the distance between the surface and the first vessel the excitation light meets. In many of the cases in Fig. 4, for example, the excitation photons scatter down to $40\,\mu$m before encountering a blood vessel. Penetration depth is therefore a difficult subject to speak about in absolute terms, as it strongly depends on the location of the vasculature in relation to the source excitation beam. Techniques that utilize depth selection independently of illumination, such as confocal methods, would benefit from taking this observation into consideration.

4.3. Intra-vessel distribution of fluorescence emission

At 415 nm, seen in Fig. 6(c), the intra-vessel absorption was high enough to completely prevent the excitation light from penetrating through to deeper tissues. The absorption also prevented the excitation light from being able to sample the entire vessel. This could affect measurements where an average across the vessel diameter would provide a more accurate measurement of a given parameter than just the value near the vessel wall. The 524 nm illumination light was able to sample the entire vessel, but at smaller vessel sizes the light also penetrated through the vessel and sampled a significant amount of tissue outside the vessel in question. At 800 nm, the results are similar to what to the 524 nm excitation case in Fig. 6(b), though as expected more light is able to penetrate through the vessel. Note that while these results demonstrate that using 415 nm illumination can allow for strong emphasis of surface vasculature in the targeted illumination scheme, Fig. 4 also suggests that using this wavelength can allow for emphasized surface vasculature in all three of the illumination and detection schemes evaluated. It is worthy to note, however, that lower excitation wavelengths are associated with increased phototoxicity, as well as excitation of endogenous fluorescence.

5. Conclusion

In this paper, we showed that using a homogeneous geometry assumption to approximate the depth-distribution of the collected fluorescence signal is not an accurate for vascular fluorescence measurements. A more complex model, involving the size, concentration and position of the microvasculature being imaged, the difference in absorption between the excitation and emission wavelengths, and the difference in absorption coefficients in the fluorescing region compared to the non-fluorescing region is required to provide a more accurate picture of depth penetration.

We also examined three illumination and detection schemes used in fluorescence imaging. The targeted and confocal illumination schemes offer a more focused signal distribution over wide field illumination. Using the confocal illumination and detection scheme in particular offers very strong localization of signal to the surface vasculature, while the wide-area detection in the targeted scheme can provide more depth-weighted signals. Using the camera scheme offers the greatest depth weighting of the three illumination and detection schemes we evaluated, but at the cost of including fluorescence from near the surface over the entire illumination region.

Lastly, we examined intra-vessel sampling and demonstrated that when using an excitation wavelength that is strongly absorbed by blood, our collected signal originates from only the top-surface of the targeted vessels. This may need to be taken into account if using a lifetime imaging method that will produce different results near the vessel walls–a wavelength which is absorbed by blood less may be more useful to provide a signal which is integrated across the vessel diameter.